3-D Nonisothermal Flow Simulation Model for Injected Pultrusion Processes

I. Mustafa, B. Khomami, and J. L. Kardos
Dept. of Chemical Engineering and Materials Research Laboratory, Washington University, St. Louis, MO 63130

Injected pultrusion (IP) is an efficient process for high-quality, low-cost, high-volume manufacturing of polymeric composites with relatively simple cross sections. This process was developed recently, and efforts to develop tools for model-based design and optimization of this process have only just begun. This work focuses on developing a 3-D nonisothermal computer simulation model for the IP process. First, the governing equations for transport of mass, momentum, and energy are formulated by using a local volume-averaging approach. In turn, a computer simulation model of the IP process is developed using the finite-element/control-volume (FE/CV) approach. Specifically, the continuity equation and the conservation of momentum equation are solved using a Galerkin FE/CV technique. The chemical species balance equation is solved in the Lagrangian frame of reference, whereas the energy equation is solved using the streamline upwind Petrov-Galerkin approach. Using the simulation model, the effect of fiber pull speed, reinforcement anisotropy, and taper of the die on the product quality was demonstrated. In addition a simple pulling-force model was developed and integrated with the simulation model. Overall, the simulation model can be effectively used to design the die geometry and to optimize the operating conditions for a given product.

Introduction

Injected pultrusion (IP) is a manufacturing process that is used to fabricate polymeric composite parts with relatively simple cross sections. In this process, fiber preforms are pulled through a die, where a thermosetting resin is injected into the fibers at a predetermined rate (Figure 1). The fiber–resin mass is then moved through a heated section at a constant speed. The resin flows through the fibrous medium, and exchanges heat with the medium and the die walls. The viscosity of the flowing resin increases due to polymerization, which in turn affects the filling profile, heat transfer, and the pulling force. At some predetermined point in the die, the resin cures to a required degree, and detaches itself from the die wall due to shrinkage. The product that comes out from the die is a composite material with a fibrous reinforcement and a polymeric matrix.

IP can be envisioned as a combination of liquid injection molding and conventional pultrusion processes. By combining the basic ideas from these two processes, several disadvantages commonly encountered in pultrusion, such as toxic solvent emissions, incapability of dealing with fast reaction chemistries, void formation, low production rates, and inconsistent fiber wet out (Dube et al., 1995), can be avoided. Thus composite parts can be made with improved mechanical and

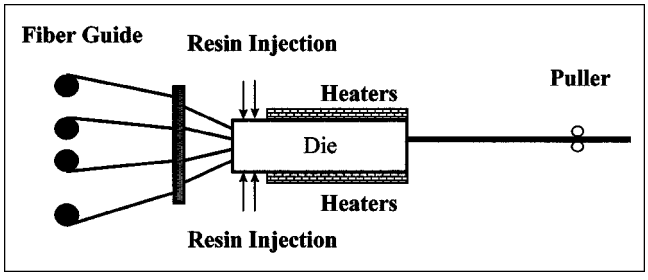

Figure 1. The injected pultrusion process.

Correspondence concerning this article should be addressed to B. Khomami.

thermal properties, less environmental concerns, and higher production rates.

The use of pultrusion processes for the manufacture of continuous polymer composites products is expanding rapidly. It has been predicted that the demand for pultruded products will grow at a rate of 11% a year (120 million pounds in 1993) and their market value will grow at a rate of 15% (Vaughan and Dillard, 1989). This substantial increase in the demand for pultruded products, as well as great emphasis on the quality of products, has forced researchers to find ways to improve and optimize this process. Both on-line and off-line investigations have been made in this regard. On-line investigations mostly employ experimental methods, based on trial-and-error and produce empirical relations that are difficult to use if either the polymer system or the geometry is changed. On the other hand, off-line investigations— mathematical modeling and simulation—provide an excellent economic alternative to on-line experimental methods. The immediate benefits to be recognized are fewer experiments, reduction in waste during experimentation, and reallocation of engineering efforts to modeling alternative process environments without hardware expenditure (Blosser et al., 1994).

The idea of injected pultrusion has only been introduced recently. Although several experiments have been performed to determine the feasibility of producing parts using injected pultrusion, only a single attempt at modeling this process has been made (Kommu et al., 1998). Although this study clearly demonstrated the utility of computer simulations in the optimization of IP processes, it is limited to modeling production of thin parts. However, IP processes, particularly with significant tapering in the injection section (i.e., in most commercial dies, the geometry is tapered downstream of the injection point to facilitate rapid attainment of a flat flow front), require a full three-dimensional (3-D) simulation model that takes into consideration the simultaneous mass/momentum/heat transfer that occurs during the fabrication process. In addition, a model to estimate the pulling force required to pull the composite through the die is also needed.

Therefore, the goal of this study was to develop a 3-D simulation model for simultaneous transfer of momentum, heat, and mass in the injected pultrusion process. The governing transport equations are developed by adopting a local volume-averaging approach. Since these equations are nonlinear and coupled, a numerical scheme based on the finite-element/control-volume (FE/CV) approach is used to construct a versatile computer simulation model. A simple pulling-force model is also developed and integrated with the 3-D flow model.

Model Formulation

Governing equations

In injected pultrusion, the resin is forced to flow through a moving fiber bed. This process can be viewed as a flow through a porous medium. It is extremely difficult to model macroscopic transport of mass, energy, and momentum in porous media based on microscopic transport models that account for variation past individual solid particles of velocity and temperature as well as other quantities of interest. Hence the governing equations are volume-averaged over a control volume. The size of this control volume is chosen in such a manner that it can represent sufficient details about both phases, that is, the fibers and the resin; but it must be small enough so that the variations in the variable of interest within the control volume are at a minimum (Khomami, 1998). The governing equations and the boundary conditions for transport of momentum, energy, and mass inside the die are then formulated by applying laws of conservation on the control volume (Khomami, 1998). Since these equations and the boundary conditions contain several parameters, it is advantageous to cast them into dimensionless form. In order to do this, one must first define the characteristic values for velocity, time, and temperature. They are as follows:

$$\hat{x}=\frac{x}{L};\quad \hat{y}=\frac{y}{W};\quad \hat{z}=\frac{z}{H};\quad \hat{t}=\frac{t}{t_{ch}};\quad \hat{t}_r=\frac{t}{t_r}$$

$$\langle\hat{u}\rangle=\frac{\langle u\rangle}{U};\quad \langle\hat{v}\rangle=\frac{\langle v\rangle}{U};\quad \langle\hat{w}\rangle=\frac{\langle w\rangle}{U}$$

$$\hat{T}=\frac{T-T_{\text{in}}}{T_{\text{wall}}-T_{\text{in}}};\quad \frac{\partial\hat{P}}{\partial\hat{x}}=\frac{\mu UL}{S_{xx}};\quad \frac{\partial\hat{P}}{\partial\hat{y}}=\frac{\mu UW^2}{S_{yy}L};$$

$$\frac{\partial\hat{P}}{\partial\hat{z}}=\frac{\mu UH^2}{S_{zz}L}, \tag{1}$$

where u, v, and w are velocities in the x, y, and z directions; P is the pressure; S is the permeability tensor; T is the temperature; U is the fiber pull speed; μ is the resin viscosity; t is the time; L is the length of the die; W is the die width; H is the die thickness; t_{ch} is the characteristic time for heat transfer; t_r is the characteristic reaction time; and $\langle\ \rangle$ represents the phase average of a quantity.

Using these dimensionless parameters, the governing equations take the following dimensionless forms:

Volume-Averaged Continuity Equation

$$\frac{\partial\langle\hat{u}\rangle^r}{\partial x}+\frac{\partial\langle\hat{v}\rangle^r}{\partial y}+\frac{\partial\langle\hat{w}\rangle^r}{\partial z}=0. \tag{2}$$

Volume-Averaged Momentum Equation

$$\begin{bmatrix}\langle\hat{u}\rangle^r\\ \langle\hat{v}\rangle^r\\ \langle\hat{w}\rangle^r\end{bmatrix}=-\begin{bmatrix}1&0&0\\0&1&0\\0&0&1\end{bmatrix}\begin{bmatrix}\dfrac{\partial\langle\hat{P}\rangle^r}{\partial\hat{x}}\\ \dfrac{\partial\langle\hat{P}\rangle^r}{\partial\hat{y}}\\ \dfrac{\partial\langle\hat{P}\rangle^r}{\partial\hat{z}}\end{bmatrix}+\epsilon_r\begin{bmatrix}1\\0\\0\end{bmatrix}. \tag{3}$$

Volume-Averaged Degree of Cure Equation

$$\frac{D\alpha}{D\hat{t}}=f\left(\langle\alpha\rangle^r,\langle\hat{T}\rangle^r\right). \tag{4}$$

Volume-Averaged Energy Equation

$$\frac{\left\{\epsilon_r(\rho C_p)_r + \epsilon_f(\rho C_p)_f\right\}}{(\rho C_p)_f}\frac{\partial\langle\hat{T}\rangle}{\partial\hat{t}} + Pe\left(\frac{\partial\langle\hat{T}\rangle}{\partial\hat{x}} + \frac{L}{W}\frac{\partial\langle\hat{T}\rangle}{\partial\hat{y}} + \frac{L}{H}\frac{\partial\langle\hat{T}\rangle}{\partial\hat{z}}\right) = \left(\frac{\partial^2\langle\hat{T}\rangle}{\partial\hat{x}^2} + \frac{L^2}{W^2}\frac{\partial^2\langle\hat{T}\rangle}{\partial\hat{y}^2} + \frac{L^2}{H^2}\frac{\partial^2\langle\hat{T}\rangle}{\partial\hat{z}^2}\right) + Br\left(\langle\hat{u}\rangle^2 + \frac{S_{xx}}{S_{yy}}\langle\hat{v}\rangle^2 + \frac{S_{xx}}{S_{zz}}\langle\hat{w}\rangle^2\right) + Da\frac{d\alpha}{d\hat{t}}, \quad (5)$$

where ϵ_r is the resin volume fraction; α is the degree of cure; ρ is the density; k is the thermal conductivity; r represents the resin phase; f represents the fiber phase; H_R is the molar heat of reaction; Pe is the Peclet number; Br is the Brinkman number; and Da is the Damköhler number. These dimensionless numbers are defined as follows:

$$Pe = \frac{UL}{\alpha_t}, \qquad Br = \frac{\mu(\alpha,T)U^2L^2}{S_{xx}\Delta T\langle k\rangle}, \qquad Da = \frac{\epsilon_r H_r \rho_r L^2}{\langle k\rangle \Delta T t_r}, \quad (6)$$

where α_t and $\langle k\rangle$ are the effective thermal diffusivity and thermal conductivity, respectively, and are defined as follows:

$$\langle k\rangle = \epsilon_r k_r + \epsilon_f k_f; \qquad \alpha_t = \frac{\langle k\rangle}{\epsilon_r(\rho C_p)_r + \epsilon_f(\rho C_p)_f}. \quad (7)$$

In deriving the preceding equations, several assumptions have been made: the fibers and the resin are in thermal equilibrium, the fluid is Newtonian, the flow is incompressible, and the densities and thermal conductivities are independent of temperature. In addition, the viscosity is assumed to be only a function of temperature and degree of cure. In this study, we have used the following equation to describe the temperature and cure dependence of the viscosity

$$\mu(\langle\alpha\rangle^r, \langle T\rangle) = \mu_0 \exp(a\langle T\rangle + b\langle\alpha\rangle^r), \quad (8)$$

where a and b are empirical constants that are evaluated experimentally. It should be noted that the previous assumptions are reasonable for resins commonly used in IP processes (Khomami, 1998).

For a typical pultrusion process the pulling speed ranges from 0.1 m/min to 1 m/min, resin injection pressures vary from 0.1 MPa to 0.5 MPa, the fibrous reinforcements are either glass or carbon, and the typical resins used are vinyl esters, polyesters, and epoxies (Meyer, 1985). The fiber-volume fractions typically range between 0.5 and 0.6, and the typical permeability values are usually in the range of 10^{-9} to 10^{-11} m^2. On the basis of these values, the range of Pe, Br, and Da numbers routinely encountered in IP processes have been estimated and are shown in Table 1.

Table 1. Range of Dimensionless Groups

Dimensionless Group	Range
Peclet number	1–50
Brinkman number	0.1–1.5
Damköhler number	1–10

Boundary conditions

In order to solve the preceding set of equations, one needs to specify the boundary conditions. The appropriate boundary conditions for these differential equations are as follows:

Momentum-Balance Boundary Conditions

$$\langle\hat{V}\rangle^r \cdot n = 0 \qquad \text{on all solid walls.} \quad (9)$$

$$\hat{P} = \frac{P_{\text{in}}S}{\mu LV} \qquad \text{inlet pressure specified.} \quad (10)$$

or

$$\langle\hat{V}\rangle^r \cdot n = \frac{V_{\text{in}}}{U} \qquad \text{inlet flow rate specified.} \quad (11)$$

Energy-Balance Boundary Conditions

$$\langle\hat{T}\rangle_{\text{wall}} = 1 \quad \text{on all solid walls} \quad \text{or} \quad \left.\frac{\partial\hat{T}}{\partial n}\right|_{\text{wall}} = \text{specified.} \quad (12)$$

$$\langle\hat{T}\rangle_{\text{in}} = 0 \qquad T_{\text{in}} = T_{\text{resin}}. \quad (13)$$

$$\frac{\langle\partial\hat{T}\rangle}{\partial n} = 0 \qquad \text{no heat flux at the moving front.} \quad (14)$$

Species-Balance Initial and Boundary Conditions

$$\alpha_{\text{initial}} = 0. \quad (15)$$

$$\frac{\partial\alpha}{\partial n} = 0 \qquad \text{at the die wall and the moving front.} \quad (16)$$

Pulling-force model

To date, a few simple pulling-force models for the pultrusion process have been proposed (Batch, 1989; Cai and Gutowski, 1992). These models take into account the drag force resulting from compaction drag in the taper section of the die, which has contributions from elastic fiber forces and pressure forces, as well as solid–solid friction in the region of the die where the resin has gelled. Specifically, it has been shown that solid–solid friction is the dominant drag force (Batch, 1989). Moreover, it has been demonstrated that the contribution of fiber-elastic forces to compaction drag is generally negligible for fiber bundles used in pultrusion or injected pultrusion processes (Cai and Gutowski, 1992). Since in injected pultrusion one does not generally want to have the fluid gel in the mold in our model we have not taken into

account solid–solid friction. Moreover, the effect of fiber-elastic forces on compaction drag has been neglected. However, we have included the effect of viscous drag that is expected to play a significant role in determining the overall drag when solid–solid friction is not present.

Viscous Drag. Viscous drag arises when a thin layer of resin is sheared between the fibers and the die wall. This resistance can be modeled by considering a plane Couette flow with the bottom plate moving at a constant pull speed (i.e., a stationary boundary and a moving fiber):

$$F_{\text{viscous}} = \frac{2U}{\lambda}\int_0^{\text{gelpoint}} \{w + h(x)\}\,\mu(\langle \alpha^r \rangle, \langle T \rangle)\,dx, \quad (17)$$

where λ is the thickness of the resin between the solid boundary and the fiber adjacent to the wall. It should be noted this quantity can be estimated by taking the square root of the permeability.

Compaction Drag. Compaction drag exists mainly in the tapered section of the die, and it depends strongly on the resin pressure and the fiber-elastic forces. Neglecting fiber-elastic forces, the compaction drag can be calculated by using the following equation (Batch, 1989)

$$F_{\text{compaction}} = 2\int_0^{\text{taper length}} \{w + h(x)\}\,P(x)\sin\theta\,dx, \quad (18)$$

where P is the resin pressure and θ is the taper angle.

Numerical Scheme

In this study, the FE/CV approach has been adopted to solve the preceding system of equations. In this approach, a finite-element mesh covering the entire mold is generated (Figure 2). The mesh is constructed in such a way that more nodes are concentrated at the point of resin injection because of relatively larger pressure gradients. Then the control volumes are constructed around each node of the mesh by connecting the mid-sides of all the elements surrounding that node (Figure 3). A fill factor is assigned to each control volume. The fill factor is defined as the ratio of the volume of material in the control volume or unit cell to the total volume of the cell. The magnitude of each fill factor varies from zero to unity, zero denoting an empty control volume and one indicating a completely filled control volume (unity). The flow front is located in cells whose fill factor is between zero and unity.

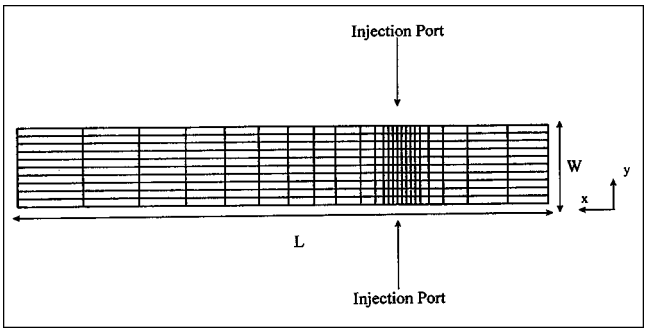

Figure 2. Representative 2-D finite-element mesh.

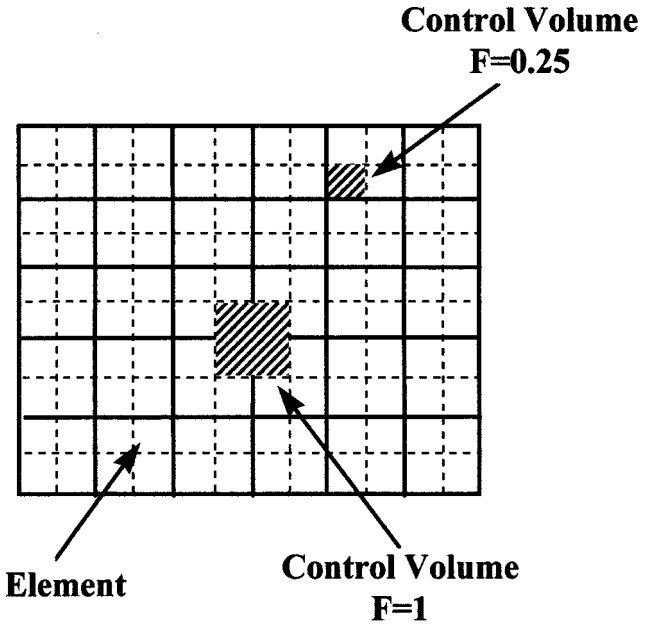

Figure 3. Finite-element/control-volume approach.

The total volume of the control volume can be calculated by adding the contributions from different elements belonging to that control volume, that is,

$$V_n = \sum V_{en}, \quad (19)$$

where V_n is the total volume of the control volume surrounding the node n, and V_{en} is the volume contribution from different elements surrounding that node. The flow rate from a control volume k to another control volume j is calculated by using

$$q_{kj} = -A_{kj}\nu_n \quad (20)$$

where A represents the area of the side of the element, and ν_n is the net velocity into the control volume. Once the flow rates between control volumes are known, the net flow Q into control volume k can be calculated as

$$Q = \sum_{j=1}^{n} q_{kj}\Delta t. \quad (21)$$

It is clear that the exact location of the flow front is not known *a priori* in the control volume approach. However, the simulation time required for this technique is significantly lower in comparison with other remeshing schemes (Kommu et al., 1998). This is an important advantage in CPU-intensive 3-D simulations. Moreover, accurate information on the position of the flow front can be obtained with the FE/CV approach during postprocessing. For example, this can be done by cal-

culating the time required to fill half of the control volume. That is, during updating of the fill factors, if the fill factor of a node changes from less than 0.5 to greater than 0.5, then the time at which it is equal to 0.5 is evaluated through linear interpolation. These half-times are then used to determine contours of constant half-time positions of the flow front during the filling process.

To solve the equations at each time step, the momentum equation (Eq. 3) is substituted into the continuity equation (Eq. 2) to get a conservation equation in terms of pressure

$$\frac{S}{\mu}\nabla^2 P = 0. \tag{22}$$

The pressure equation is then solved subject to the given boundary conditions using the Galerkin FE/CV method. In this work, we have chosen 8-noded cubic elements with trilinear shape functions (Pepper and Heinrich, 1992) to discretize the 3-D domain. The selection of trilinear shape functions facilitate the implementation of the control-volume approach. Thus the pressure within each cubic element can be approximated as follows:

$$P = \sum_{i=1}^{8} P_i N_i, \tag{23}$$

where N represents the shape functions, and P the unknown pressures at the nodal points. The preceding equation is substituted into the pressure equation (i.e., Eq. 22). After the pressures are calculated, the velocities are retrieved using Darcy's law (Eq. 3) from the known pressure gradients. The flow rates are calculated from the velocities, and then the time step to fill one control volume is estimated. Then the energy and species conservation equations are solved during that time step to determine the temperature and cure distribution.

The energy-balance equation is solved by using a Eulerian approach. Because of the convection term appearing in the energy-balance equation, the Galerkin discretization, which has been developed for elliptic equations, can give rise to spurious oscillations if the cell Peclet number is high. This problem is circumvented by using the streamline upwind Petrov–Galerkin (SUPG) technique, which has been developed for discretization of hyperbolic equations. The weighting functions for the SUPG technique are defined as follows (Pepper and Heinrich, 1992):

$$W_i = N_i + h\frac{\boldsymbol{\nu}\cdot\nabla N_i}{\|\boldsymbol{\nu}\|}, \tag{24}$$

where h is the characteristic element size; ν is the velocity at the centroid of the element; and N_i represents the trilinear shape functions. We have chosen the SUPG technique to discretize the energy equation because it was shown by Kommu et al. (1998) to be more cost-effective and accurate compared to the streamline upwind method (SU).

The species-conservation equation, which is also hyperbolic in nature, is solved in the Lagrangian frame of reference. The Lagrangian method is chosen because it produces the best solution for a given CPU time (Kommu et al., 1998) in comparison with the SU and the SUPG schemes. Using this approach, the species conservation equation takes the following form:

$$\frac{D\alpha}{Dt} = f(\langle\alpha\rangle^r, \langle T\rangle). \tag{25}$$

In discretized form, using a forward difference method, Eq. 25 can be written as follows:

$$\frac{(\alpha^{\text{new}} - \alpha^{\text{old}})}{\Delta t} = f\left(\langle\alpha\rangle^{\text{old}}, \langle\hat{T}\rangle^{\text{old}}\right). \tag{26}$$

Rearranging, the equation reads

$$\alpha^{\text{new}} = \alpha^{\text{old}} + f\left(\langle\alpha\rangle^{\text{old}}, \langle\hat{T}\rangle^{\text{old}}\right) dt. \tag{27}$$

The source term $f(\alpha, t)$ represents the kinetics of the curing reaction, and has been assumed to have the following general form (Kamal and Sourour, 1973):

$$f\left(\langle\alpha\rangle^r, T_0\right) = \left(K_1 + K_2\langle\alpha\rangle^r\right)\left(1 - \langle\alpha\rangle^r\right)^2, \tag{28}$$

where K_1 and K_2 have an Arrhenius dependence on temperature. Equation 28 was chosen because it can represent the reaction kinetics of the majority of the resins used in IP.

The energy-balance equation and the degree-of-cure equation are coupled, so an iterative scheme is employed for their solution. At time equal to zero, the initial temperature and the degree of cure distributions are specified and the viscosity is determined using Eq. 8. Next, the pressure distribution in the die is estimated by solving Eq. 22. Then the energy and species balance equations are solved. The energy equation is solved using an implicit forward difference approach that is unconditionally stable. However, in order to accurately solve both the energy and species balance equations, the following criterion should be satisfied (Kommu et al., 1998),

$$\frac{0.005}{d\alpha/dt} \le \Delta t \le \frac{0.02}{(d\alpha/dt)}. \tag{29}$$

The preceding criterion was developed to ensure that a minimum of 0.5% conversion is obtained in one time step. This will avoid the potential ill-conditioning of the stiffness matrix of the energy equation. On the other hand, a maximum conversion of 2% is desired in one time step. This is because time is discretized using forward differences, hence, a linear interpolation is used to approximate the cure kinetics in each time step. Therefore, if the amount of cure in one time step is too large, the linear approximation might not be accurate, and, depending upon the shape of the cure kinetics curve, the amount of cure could be either underestimated or overestimated. Thus, once the time step required to fill one control volume is determined, it is further subdivided into n time substeps until the criterion given earlier is met. Then the energy and species balance equations are solved for n time substeps. It should be noted that depending upon the cure

kinetics of the resin used, one might have to change the upper limits in Eq. 28, but this can be accomplished by simply inputting new limits into the simulation code.

The discretizations of the pressure and energy equations give rise to a set of linear and nonlinear algebraic equations, respectively. The solution of nonlinear equations requires their linearization. In this study, the Newton-Raphson method is used to provide a system of linear equations that must be solved iteratively until convergence of the solution is obtained. To solve these algebraic equations, we have used a commercially available solver (SMPAK, 1990). This solver is specially designed for solving sparsely populated matrices. To obtain convergent solutions at each time step, first the viscosity of the resin at a temperature corresponding to time t is used to solve for the velocities at $t + \Delta t$. Then the resin velocity is used to solve for the temperature and degree of cure at $t + \Delta t$. Once the degree of cure and temperature have been determined at $t + \Delta t$, the process continues until a converged viscosity is achieved. Upon convergence, the fill factors are updated using the calculated flow rates, and the procedure is repeated.

The 3-D nonisothermal and pulling force models have been integrated together as follows: first, using the computed degree-of-cure distribution, the gel-point location is determined. As mentioned earlier, however, we do not consider situations where the gel point occurs inside the die. Hence, the viscosity variation at the walls as a function of distance from the exit is computed and passed on to the viscous drag model. Then, the bulk compaction is calculated in the tapered section of the die by substituting the computed pressures in the bulk compaction model. Finally, the overall pulling force is computed by combining both the viscous drag and compaction forces.

Results and Discussions

Solution quality

In order to check the validity of the simulation code, we have compared our simulation results with analytical solutions for the species balance and the energy-balance equations in cases where the flow is 1-D and the resin has constant material properties.

In order to solve the chemical species balance equation numerically, a simple 1-D isothermal problem was formulated. In this case, the resin is injected at a constant flow rate and a constant temperature T_0 into a rectangular mold, which is also held at T_0 (Figure 4). The species balance equation takes the following form:

$$\frac{D\alpha}{Dt} = f\left(\langle \alpha \rangle^r, T_0\right) = (1-\alpha)^2\left(K_1 + K_2\alpha\right) \qquad (30)$$

Since the temperature is constant, K_1 and K_2 are also constant. Hence, the preceding ordinary differential equation can be easily solved analytically. We will first compare the analytical solution with two different numerical solutions to the problem. In the first case, we generated a rectangular mesh of 264 elements and 315 nodes and employed no division of the time step; that is, we did not include the criterion outlined in Eq. 29. As indicated by Figure 5, the numerical

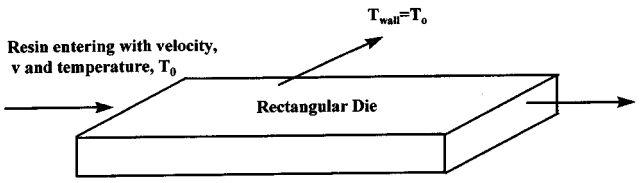

Figure 4. Test geometry for determining the accuracy of various numerical discretization techniques.

solution is not very accurate. The reason is that the cure kinetics are not accurately integrated when the division of the time step is not employed. In this case, the computer code underestimates the degree of cure. In the second case, for the same mesh, we divided the time step by invoking the criterion outlined in Eq. 29. Using this procedure we can obtain the exact solution (Figure 5). Thus, these two cases support the argument that by employing the Δt division, accurate numerical solutions can be obtained in a computationally efficient manner. It should be noted that in order to obtain the exact solution without division of time steps, a mesh with more than 1500 nodes is required. The CPU time associated with the computation with such a mesh is an order of magnitude larger than the method based on division of time steps.

A simple one-dimensional nonisothermal problem is used to examine the accuracy of the SUPG scheme used to solve the energy equation. In this case, the mold walls are set at a constant temperature T_w. The resin is injected at a constant flow rate, and at a constant temperature T_0 into the die. At some point in the die, an exothermic reaction takes place and heat is generated by the resin. At steady state, the energy-balance equation becomes a second-order ordinary differential equation with constant coefficients, which can be solved analytically. In order to check the accuracy of our code, we have compared the analytical solution with numerical solutions with the SUPG technique (Figure 6). The finite element used to generate the top figure contained 315 nodes and 264 elements. The Peclet number was taken as 10. As can be seen from the figure, a more refined mesh is required to obtain an

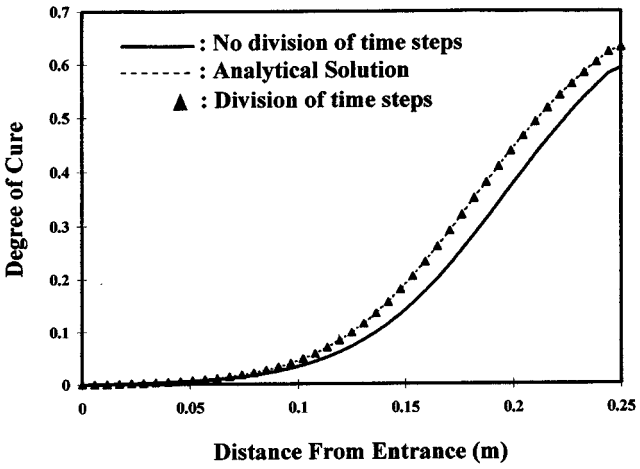

Figure 5. Degree of cure profiles for an isothermal 1-D flow using the Lagrangian approach.

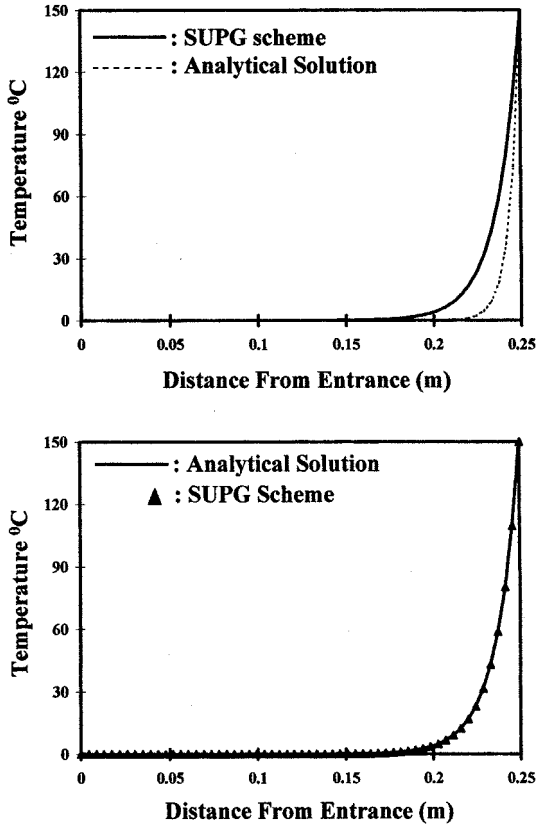

Figure 6. Temperature profile in a die at constant wall temperature.

Top, 315 nodes; bottom, 1,575 nodes.

accurate numerical prediction. This has been accomplished by increasing the number of nodes from 315 to 3896. A perfect match between the analytical and numerical results is obtained in meshes with node numbers above 1500. This is illustrated in the bottom of Figure 6.

Robustness of the simulation algorithm

In Table 1 the ranges of various dimensionless numbers for a typical pultrusion process have been shown. Any versatile simulation code must be able to simulate the IP process in the entire parameter space. In order to check the robustness of our code over the entire range of operating conditions, a number of simulations were carried out. Specifically, we considered a 3-D rectangular die (Figure 7) into which an epoxy resin (Hercules 3501-6; Lee et al., 1982) was injected at a constant flow rate of 0.0025 m^3/s and at a constant temperature of 80°C. At the same time, the carbon fibers were pulled through the die at a constant speed. The die wall temperature was set at 150°C. Under these conditions, varying the pull speed of the fibers and the reaction kinetics of the resin gave rise to the different values of the dimensionless groups mentioned in Table 1. The results of these simulations are shown in Figures 8–10.

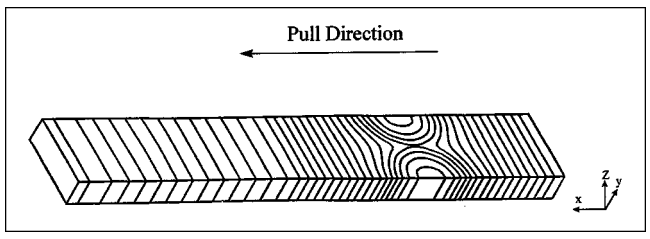

Figure 7. Typical flow-front progression under isothermal conditions.

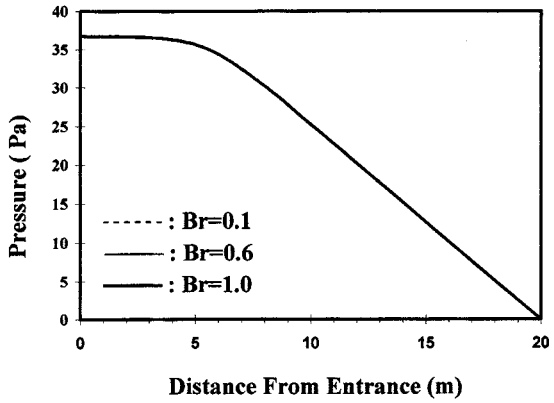

Figure 8. Typical pressure distribution at the center of the flow channel as a function of Brinkman number.

Figure 8 shows the effect of varying the Brinkman number on the pressure distribution of the resin inside the die. This figure clearly demonstrates (all the curves superimpose) that the effect of viscous dissipation is virtually insignificant under typical processing conditions. Figure 9 shows the temperature distribution inside the die at different Peclet numbers. Again three values of the Peclet number are chosen by varying the pull speed. Clearly, at high Peclet numbers, or at high pull speeds, the energy transfer is dominated by convection. Figure 10 shows the effect on the degree of cure distribution of varying the Damköhler number (the extent to which the

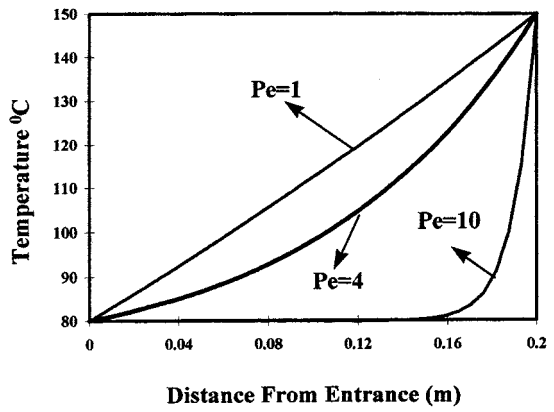

Figure 9. Typical temperature profiles at the center of the flow channel as a function of Peclet number.

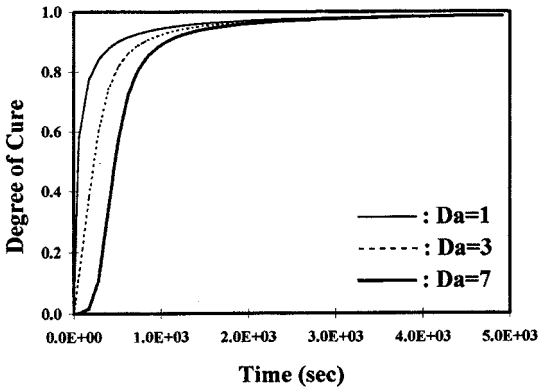

Figure 10. Typical cure profiles at the center of the flow channel as a function of Damköhler number.

heat of reaction is important). The Damköhler number was calculated by considering the characteristic time for the reaction to be the time required for the resin to cure up to 50%. The cure kinetics relation developed by Kamal and Sourour (1973) was used in these simulations, since it represents typical cure kinetics for the thermoset resins used in the IP process. As shown by Figure 10, the reaction kinetics are among the dictating variables in the process. It should be noted that mesh convergence studies were performed, and the results presented in Figures 8–10 are mesh converged.

Isothermal filling

Figures 8–10 indicate the capability of the code developed in this study to simulate the IP process over a wide range of operating conditions. In this section, we present the results of simulations for isothermal mold filling, to demonstrate the type of flow fronts that one would expect to observe under differing processing conditions. We have selected a typical pultrusion die (shown in Figure 11), which has dimensions of 0.3 m by 0.05 m by 0.01 m. A Newtonian resin with a viscosity of 1832 kg/m·s at 80°C was used, whereas the permeability of the isotropic fiber bundle was taken as 1.0 Darcy. The resin was injected into the die from two injection gates at a constant flow rate of 0.00025 m^3/s. The progression of the flow front during die filling for a pull speed of 0.00003 m/s is presented in Figure 11a. Since the permeabilities are equal in all directions, the flow contours are circular near the injection point. At the center of the die the two flow fronts meet and move toward the back and the front ends of the die. The total filling time is 4000 s. As can be seen from Figure 11a, there is an enormous back flow out the rear of the die. To avoid this flow, the fiber pull speed was increased from 0.00003 m/s to 0.03 m/s. As is evident from Figure 11b, the higher pull speed has resulted in no back flow; however, this pull speed is too high for the given system, since it has created a big void in the center of the composite. Obviously, this situation is also undesirable because poor mechanical properties will result. An optimum pull speed is therefore needed so that the fibers are fully wetted and a flat flow front is obtained prior to the curing section, with no leakage occurring out the back. This optimum pull speed is shown in Figure 11c where very closely spaced flow fronts in the rear end of the die are indicative of no back flow. The optimum fiber pull speed was determined to be 0.0017 m/s.

In order to demonstrate the effect of changing fiber bundle permeability on the position of the flow front, we have performed simulations with various permeabilities along the principal directions. Figure 12a shows the results of a simulation where the permeabilities of the carbon fiber bundle are equal in all three directions. Circular flow fronts are thus obtained around the entry points. Figure 12b shows the condition where $S_{xx} = 5S_{yy} = 5S_{zz}$. The figure clearly shows the relative ease of resin movement in the x-direction as compared to the y and z directions. Thus flow fronts are highly elliptic in shape near the injection point. Clearly, for a fiber/resin system with high permeability in the x-direction, a lower pull speed is required to pull the composite in order to avoid formation of a void in the center of the part. However, the pull speed at which leakage occurs out the back also increases. In Figure 12c, the permeabilities are assumed to be

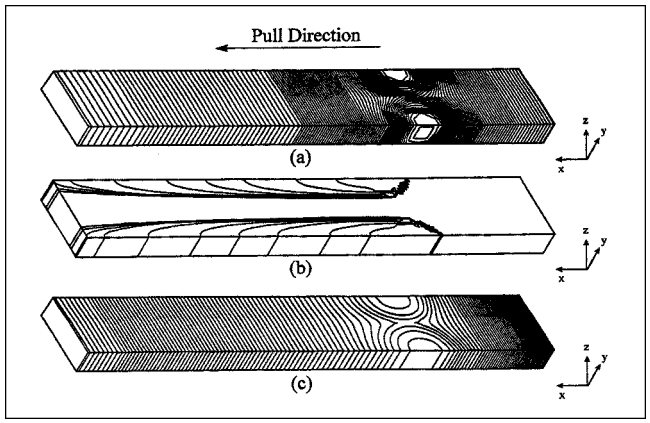

Figure 11. Sample isothermal simulation of the IP process.

(a) Flow-front progression with excess back flow; (b) flow-front progression showing formation of a void; (c) flow-front progression under optimal conditions.

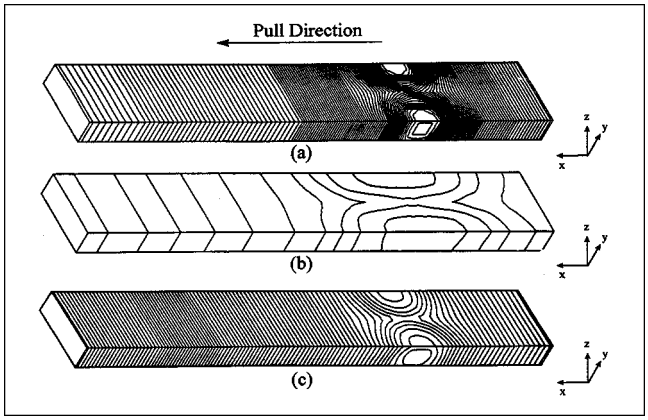

Figure 12. Effect of preform permeability on flow-front progressions.

(a) Isotropic preform; (b) anisotropic preform, $S_{xx} = 5S_{yy} = 5S_{zz}$; (c) anisotropic preform, $S_{xx} = S_{yy} = 2S_{zz}$.

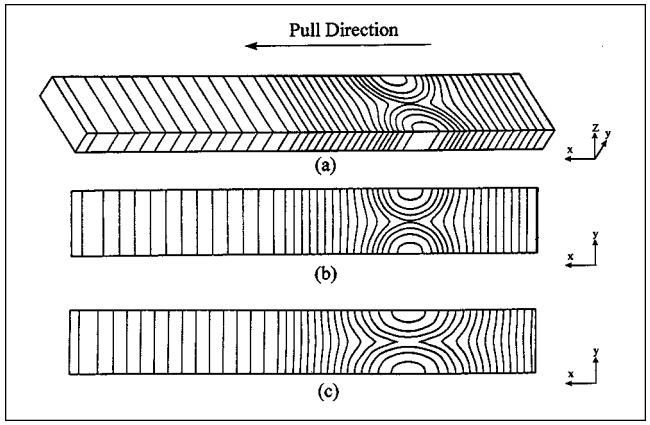

Figure 13. Comparison of 2-D and 3-D simulation results.

(a) Three-dimensional flow-front progressions for a part with a small thickness [$(W/H) \geq 5$]; (b) 2-D flow-front progression for a part with a small thickness [$(W/H) \geq 5$]; (c) top view of a 3-D flow-front progression for a part with a large thickness [$(W/H) \leq 5$].

$S_{xx} = S_{yy} = 2S_{zz}$, in which case the resin permeates faster in the x and y directions as compared to the z direction. The shape of the flow fronts changes accordingly.

In order to determine under what conditions more cost-efficient 2-D simulation can be used, we compared the results of 2-D and 3-D simulations. Figures 13a and 13b show the flow fronts for 3-D and 2-D rectangular mold filling, respectively. In both cases the process conditions and physical properties of the fiber bundle and the permeant are kept exactly the same. Specifically, a mold with dimensions of 0.20 m by 0.05 m by 0.01 m was used and the resin was injected at a constant flow rate and at a constant temperature from two opposite locations, and the fiber pull speed was taken as zero. As can be seen from Figures 13a and 13b, the flow contour plots resulting from 2-D and 3-D simulations are exactly the same for this thin-section geometry. As the thickness of the die is increased from 0.01 to 0.1 m, however, the flow fronts predicted by the 3-D simulations significantly deviate from the flow fronts predicted from the 2-D simulation with a die thickness of 0.01 m (see Figure 13c). Since, in a 2-D simulation, the equations are averaged along the thickness of the die, changing the thickness from 0.01 m to 0.1 m while maintaining the 2-D flow rate (i.e., flow rate per unit height) does not result in any change in the flow fronts; however, this is not the case for a full 3-D simulation. Based on these types of simulations, we have been able to demonstrate that if the thickness of the die is at least five times less than the width of the die, the 2-D approximation is adequate. Hence, for thick parts a full 3-D simulation is required. The results presented in this section are mesh converged. In general, once we reach a discretization level where the results for two meshes are within 2% of one another, we consider the results to be mesh converged.

Effect of taper angle

In prior work (Kommu et al., 1998), it was shown that for thin cavities, the pressure gradient in the thickness direction is negligible compared to the pressure gradient in the major plane of the cavity; but if one considers the tapering of the test section in the flow direction of the injection section of the die, the magnitude of the pressure gradient in the z-direction (i.e., thickness direction) becomes more significant as the taper angle is increased. This makes using a 2-D code for high taper angles questionable. To compensate for this inaccuracy, Kommu et al. (1998) approximated the pressure gradient in the thickness direction as follows:

$$\frac{\partial \langle P_r \rangle^r / \partial z}{\partial \langle P_r \rangle^r / \partial y} \approx \frac{\Delta P_z W}{\Delta P_y H} = \frac{H S_{yy}}{W S_{zz}}. \tag{32}$$

To examine the accuracy of this approximation, we have performed full 3-D simulations for dies with taper angles of 2°, 5°, and 10°, and have compared our simulation results with predictions of 2-D simulations coupled with the preceding equation. This comparison is shown in Figure 14. Clearly, as taper angle is increased, the predictions from approximated 3-D pressure distributions show increased deviation from that of the rigorous 3-D simulations. At a taper angle of 10° this deviation is significant (Figure 14c), and thus the use of a 2-D code in conjunction with Eq. 32 to approximate the pressure in the taper region at taper angles greater than 10°, even for a relatively thin part, is not recommended. As pointed out earlier, the magnitude of pressure in the taper section plays a significant role in determining the compaction drag. So, in dies with significant taper it is essential to perform 3-D simulations in order to correctly estimate the required pull force to drag the composite at a given velocity.

Mesh-converged flow-front contours as a function of taper angle (2°, 5°, and 10°) are shown in Figure 15. The flow fronts are plotted at the same time increments. Figure 15 demonstrates that a flat flow front is more rapidly attained as the taper angle is increased. This in turn leads to minimization of void formation as well as to the shortening of the required length of the die. Although increasing the taper angle aids in quick attainment of a flat flow front, which results in reduction of the total required die length, it also leads to an increase in the pulling force required to pull the product (see the following subsection on pulling-force estimation). Hence, one must in general optimize the degree of taper such that the desired product can be made with the optimum die length and pull force.

Nonisothermal filling

In practice, the injection pultrusion process is nonisothermal. It is therefore important to examine the capillary of the code to perform nonisothermal simulations. To do this, we present sample simulation results for a rectangular die with and without taper. In the first case, we performed nonisothermal simulations for a rectangular injected pultrusion die (Figure 16). The die has dimensions of 2.0 m by 0.3 m by 0.1 m. An epoxy resin (Hercules 3501-6) was injected into the die from two opposite locations at a constant flow rate of 0.00025 m^3/s. At the same time, the carbon-fiber bundles were pulled at an optimum pull speed of 0.0017 m/s. Under these conditions, there is no back flow from the rear end of the die and the flow front is flat prior to entering the curing section

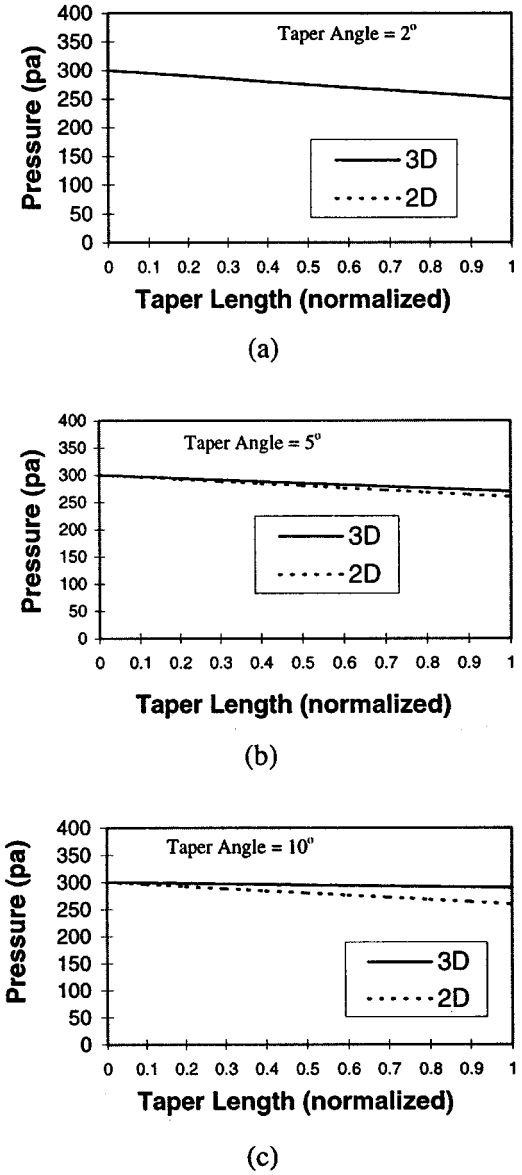

Figure 14. Comparison of pressure profiles predicted by the 2-D and 3-D simulation models in the injection section as a function of taper angle.

L is the fraction of the total length of the injection section: (a) 2° taper angle; (b) 5° taper angle; (c) 10° taper angle.

(Figure 16). As mentioned earlier, at this optimum condition, the fibers are completely wet and a uniform degree of cure can be achieved. It should be noted that the permeability of a carbon fiber bundle has been obtained from (Skartsis et al., 1992)

$$S_{xx} = \frac{\epsilon_r^2}{(1-\epsilon_r)^2} \times 4 \times 10^{-12} \tag{33}$$

$$S_{yy} = 64 \times 10^{-11} \times 10^{(4.75\epsilon_r - 4.275)}. \tag{34}$$

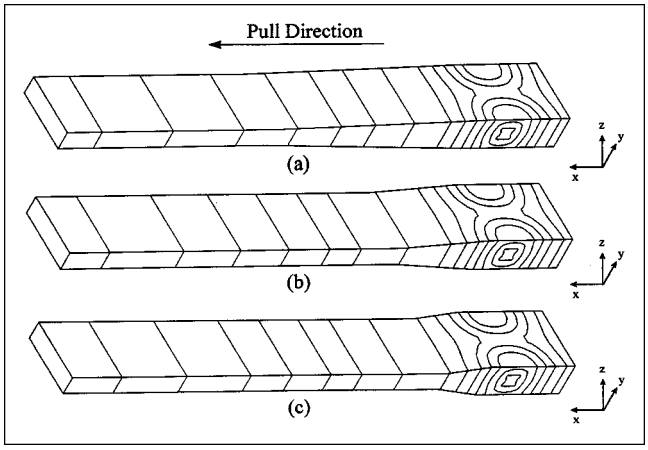

Figure 15. Effect of taper angle on the flow-front progression.

(a) 2° taper angle; (b) 5° taper angle; (c) 10° taper angle.

In addition, we have set $S_{yy} = S_{zz}$, and the porosity, ϵ_f, of the fiber bed (the resin volume fraction) was taken as 0.5. Lee et al. (1982) have determined that the resin viscosity can be described as follows:

$$\langle \mu \rangle^r = \mu_0 \exp\left(\frac{E}{RT} + W \langle \alpha \rangle^r \right), \tag{35}$$

where $\mu_0 = 7 \times 10^{-14}$ Pa·s, $E = 9 \times 10^4$ J/mol, $R = 8.314$ J/mol·K, and $W = 14.1$. The heat of reaction for this epoxy resin is 473.6 J/mol (Lee et al., 1982). In addition to this, the cure kinetics for this epoxy resin (Hercules 3501-6) are given as follows (Lee et al., 1982):

$$f(\alpha, T) = (K_1 + K_2 \alpha)(1-\alpha)(B-\alpha) \quad \alpha \le 0.3 \tag{36}$$

$$f(\alpha, T) = K_3(1-\alpha) \quad \alpha \ge 0.3, \tag{37}$$

where $K_i = A_i \exp(-\Delta E_i/RT)$, $i = 1, 2, 3$, and B is a constant that is determined through a fitting procedure. Tables 2 and 3 summarize the values used in the simulation.

Mesh-converged simulation results for temperature and degree-of-cure profiles for this resin/fiber system at the optimum condition are shown in Figure 17. As shown in the top of Figure 17, the wall temperature in the curing section is

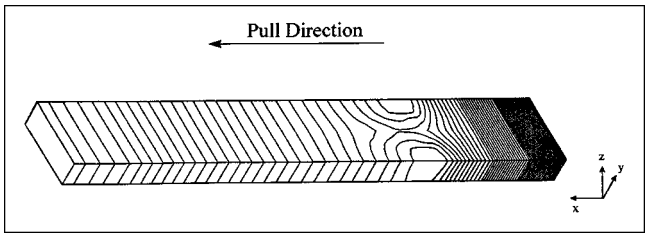

Figure 16. Flow-front progression under optimal processing conditions.

Table 2. Material Properties of Hercules Resin and Carbon Fiber

Material Properties	Values
Density of resin	1.274 g/cm^3
Density of fiber	1.37 g/cm^3
Heat capacity of resin	0.468 cal/g·°C
Heat capacity of fiber	0.92 cal/g·°C
Thermal conductivity of resin	0.000385 cal/cm·s·°C
Thermal conductivity of fiber (transverse)	0.006 cal/cm·s·°C

maintained at 150°C. A parabolic temperature profile is observed in the thickness direction at the midpoint of the *xy* plane, indicating diffusion-controlled heat transfer. Along the flow direction (*x*-direction), the temperature at the midpoint of the *zy* plane is increased from 80°C, which is the incoming resin temperature, to 150°C at the exit. Obviously, along the flow direction the heat transfer is convection dominated. At the injection point, the degree of cure is assumed zero, whereas at the exit the required value of 50% is obtained. Hence obtaining a void-free composite with 50% degree of cure in the product was achieved by varying the resin pressure, the fiber pull speed, and the temperature of the wall.

Next we simulated nonisothermal mold filling of a die with a tapered section near the injection point. The die has dimensions of 1.5 m by 0.2 m by 0.1 m, and the taper angle is 5°. For this simulation-condition, mesh-converged flow fronts under the optimum condition are shown in Figure 18, while Figure 19 shows the mesh-converged temperature and degree-of-cure profiles, respectively. The optimum pull speed in this case, for a degree of cure, 0.55, was estimated to be 0.012 m/s. Clearly, by using a die with a tapered section, flat flow fronts can be achieved quickly, resulting in a higher production rate.

Pulling-force estimation

For the same fiber/resin system previously used, we also estimated the required pulling force. The resin was injected from two opposite locations into three different dies with taper angles 0°, 2°, and 5°, respectively. At the same time, the carbon fibers were pulled at a constant velocity. The test geometry had dimensions of 1.5 m by 0.2 m by 0.1 m. By adjusting the flow rate of the resin and the die wall temperature, three different pulling speeds were selected, such that the resin cures to 55% at the die exit. It is important to have

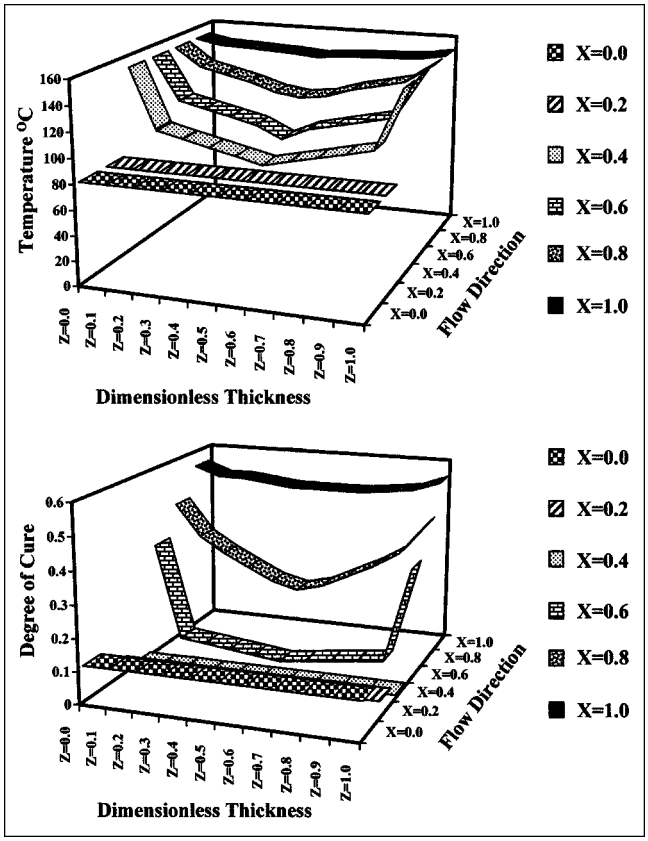

Figure 17. Temperature and degree of cure profiles.

Top: temperature profile at the midplane of the die; bottom: degree of cure profile at the midplane of the die.

optimum curing at the die exit; otherwise, a tremendous pulling force will be required if the resin cures completely inside the die. By adopting this approach, the frictional drag force can be ignored. Thus we estimated the viscous drag force and the drag force due to compaction of the fibers in the tapered section of the die. The results are shown in Figure 20. The pulling force required increases almost linearly with the pulling speed. Clearly, the total pull force required in the case of a die with zero taper angle is less than the total pull force required for dies with a taper. This is due to compaction forces present in the tapered section of the die. Moreover, as the pull speed increases, the viscous drag term

Table 3. Cure Kinetics Parameters for Hercules (3501-6) Resin

Parameter	Value
A_1	2.101×10^{9} min^{-1}
A_2	-2.014×10^{9} min^{-1}
A_3	1.960×10^{5} min^{-1}
ΔE_1	8.07×10^{4} J/mol
ΔE_2	7.78×10^{4} J/mol
ΔE_3	5.66×10^{4} J/mol
B	0.47

Source: Lee et al. (1982).

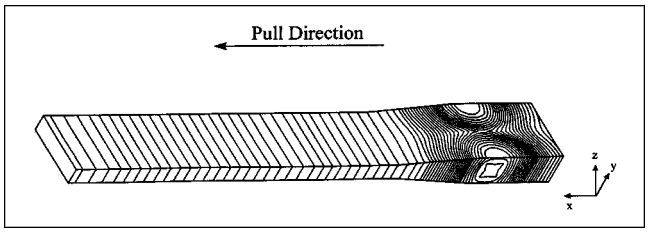

Figure 18. Flow-front progression under optimal processing conditions for a die with a tapered section.

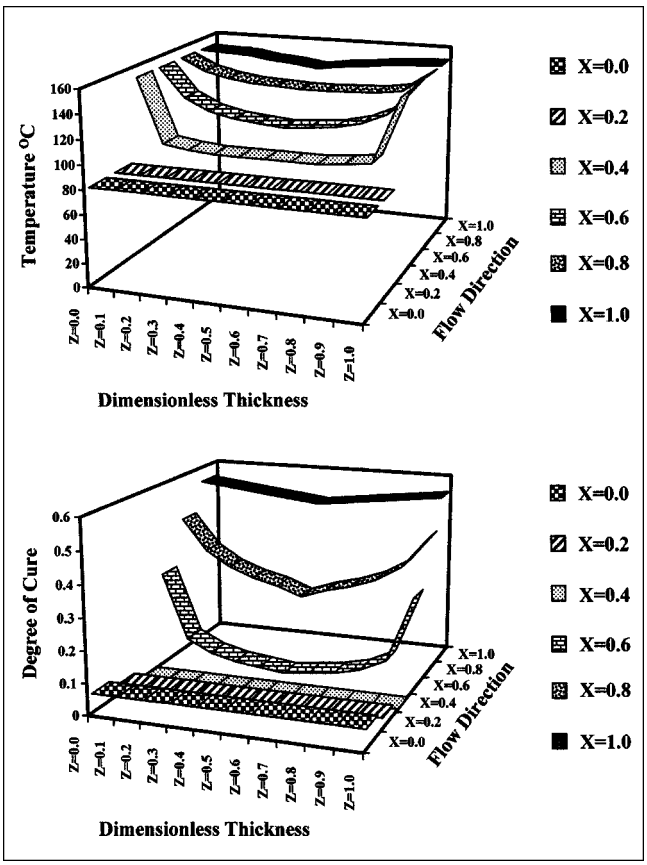

Figure 19. Temperature and degree of cure profile for a die with a tapered section.

Top: temperature profile at the midplane of a die; bottom: degree of cure profile at the midplane of the die.

is expected to become dominant; hence the compactional drag that arises due to the taper should become less significant. Thus, under conditions of high pull speed and relatively low

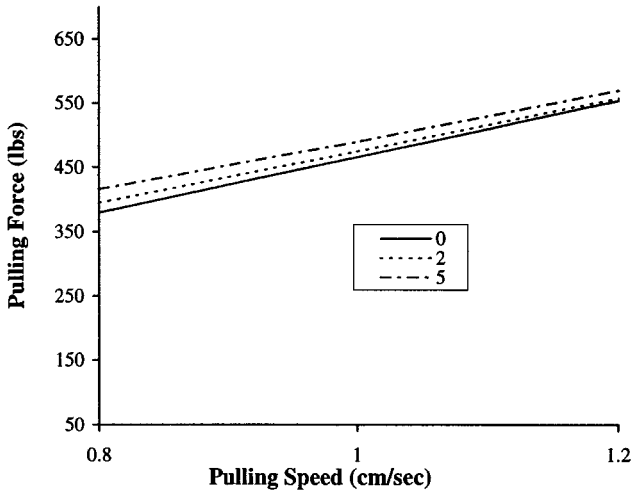

Figure 20. Pulling force as a function of pull speed for viscous die taper angles.

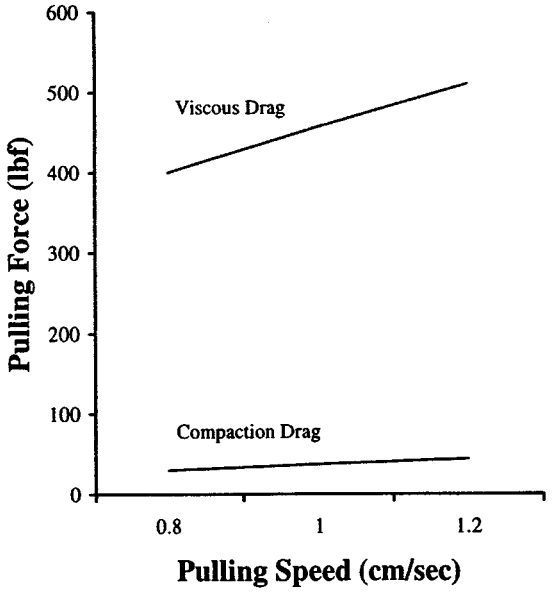

Figure 21. Contribution of viscous and compaction drags to the overall drag force as a function of pull speed.

taper angle (i.e., less than 5°), the pull force required for a die with or without taper should be very similar. Figure 21 clearly illustrates this point. In this figure the relative contribution of the viscous and compaction drag to the overall pulling force for a die with a taper angle of 5° are shown. Clearly, the viscous-drag contribution to the overall pulling force is very high compared to that of compaction drag. Thus, at relatively low taper angles the compaction-drag contribution to the overall drag force is not very significant. It should be noted that similar trends are observed for dies with taper angles of up to 10°. The verification of the pulling-force model with experimental data is currently underway in our laboratory and will be the subject of a future communication.

Conclusions

In this work a highly efficient 3-D computer simulation model for the IP process has been developed. The utility of this simulation model in design and optimization of the IP process was demonstrated through a number of example simulations. It was shown that with the aid of the simulation model the die geometry (i.e., die length, optimum location of the injection port, optimum shape of the injection section) can be designed and the operating conditions (i.e., injection pressure or flow rate, fiber pull speed, wall temperature) can be optimized. In addition, a pulling-force model was developed and incorporated into the simulation model, and it was shown that viscous drag is the dominant drag force for situations where the resin does not reach its gel point inside the die and the taper angle is in the range of 5°–10°.

Acknowledgment

This work was supported in part by the Advanced Research Project Agency under ARPA Order No. 284, Affordable Polymeric Composite Materials Synthesis and Processing Program.

Literature Cited

Batch, G. L., ''Cross Linking Free Radical Kinetics and the Pultrusion Processing of Composites,'' PhD Thesis, Univ. of Minnesota, St. Paul (1989).

Blosser, R., J. Florio, Jr., and D. Prasad, ''Continuous Resin Transfer Molding for High Quality, Low Cost, Constant Cross Section Composite Structural Elements,'' *Proc. Int. SAMPE Symp*., Society of Aerospace Material and Process Engineers (1994).

Cai, Z., and T. G. Gutowski, ''The 3-D Deformation Behavior of a Lubricated Fiber Bundle,'' *J. Comp. Mat*., **26**, 1207 (1992).

Dube, M. G., G. L. Batch, G. H. Vogel, and C. W. Macosko, ''Reaction and Injection Pultrusion of Thermoplastic and Thermoset Composites,'' *Polym. Compos*., **16**, 378 (1995).

Kamal, M. R., and S. Sourour, ''Kinetics and Thermal Characterization of Thermoset Cure,'' *Polym. Eng. Sci*., **13**, 59 (1973).

Khomami, B., ''A Unified Approach to Modeling Transport of Heat, Mass and Momentum in Processing of Polymer Matrix Composite Materials,'' *Processing of Continuous Fiber Reinforced Composites*, R. S. Dave, ed., Carl Hanser Verlag, Munchen, Germany, in press (1999).

Kommu, S., K. B. Khomami, and J. L. Kardos, ''Modeling of Injected Pultrusion Processes: A Numerical Approach,'' *Polym. Compos*., **19**, 335 (1998).

Lee, W. J., A. C. Loos, and G. S. Springer, ''Heat of Reaction, Degree of Cure, and Viscosity of Hercules 3501-6 Resin,'' *J. Comp. Mat*., **16**, 150 (1982).

Meyer, R. W., *Handbook of Pultrusion Technology*, Chapman & Hall, London (1985).

Pepper, D. W., and J. C. Heinrich, *The Finite Element Method— Basic Concepts and Applications*, Hemisphere, New York (1992).

Skartsis, L., B. Khomami, and J. L. Kardos, ''Polymeric Flow Through Fibrous Media,'' *J. Rheol*., **36**, 1377 (1992).

SMPAK Users Guide, Software Version 2.0, Manual Version 2.0, Scientific Computing Associates (1990).

Vaughan, J. G., and T. W. Dillard, ''Characterization of Pultrusion Process for Graphite/PEEK,'' *SPI Composite Institute Proc*. (1989).

Manuscript received June 23, 1998, and revision received Oct. 14, 1998.